Supplement to "Anatomy of a crustal-scale accretionary complex: Insights from deep seismic sounding of the onshore western Makran subduction zone, Iran " by Haberland et al. (G47700)

EXPERIMENT & DATA EXAMPLES

In September 2017, three 200 km long, north-south trending, crustal-scale, deep seismic sounding (DSS) profiles have been acquired along 56° E, 59.5° E and 60.75° E (Figure 1 of main document). Along each profile, 9 to 10 artificial sources (chemical explosions in boreholes) with charges between 400 and 800 kg of explosives at a borehole depth of about 30 m were shot. Along each of the sequentially measured profiles, 300 autonomous digital recorders sampling with 100 samples per seconds and equipped with 4.5 Hz vertical geophones were deployed. Thus the wavefields were densely sampled due to small inter-station distances of around 600 m (see Figure S1). Built-in GPS secured the accurate timing of the recordings. More information about the experiment and the data can be found in Haberland et al. (2020).

MARKOV CHAIN MONTE CARLO TRAVEL TIME TOMOGRAPHY

We apply a Bayesian Markov chain Monte Carlo formalism (McMC) to the inversion of refraction seismic, travel time data sets to derive 2D velocity models below lines of sources and seismic receivers (Ryberg & Haberland, 2018). Typical refraction data sets have experimental geometries which are very poor, highly ill-posed and far from being ideal, and thus structural resolution quickly degrades with depth. Conventional inversion techniques, based on regularization, potentially suffer from the choice of inappropriate inversion parameters and only local model space exploration. Markov chain Monte Carlo techniques (Bodin & Sambridge, 2009, Bodin et al., 2012) are used for exhaustive sampling of the model space without the need of prior knowledge (or assumptions) of inversion parameters, resulting in a large number of models fitting the observations. Statistical analysis of these models allows to derive an average (reference) solution and its standard deviation, thus providing uncertainty estimates of the inversion result. We checked the results obtained from the McMC method by also applying a conventional inversion code based on a regularized inversion (e.g., Zelt & Barton, 1998). Comparison of the models derived by the two different inversion approaches shows a very good agreement.

Input data for the algorithm are the travel times of the Pg and Pn phases (first arrivals) along each profile, which were manually picked after the data had been bandpass-filtered and appropriately scaled. In total, 1823, 1921 and 2150 travel time picks could be used for the calculations for profiles 1, 2 and 3, respectively (Figure S2). The velocity models of the three profiles are shown in Figure 2 of the main text and Figures S3 to S5. Figure S6 shows the uncertainties/errors of the models. In order to assess the accuracy of the derived models we conducted synthetic recovery tests (Figure S7).

REFLECTION SEISMICS – LINE DRAWING MIGRATION

Given the dense spacing of seismic receivers (~600 m), reflections from crustal and upper mantle discontinuities could be recorded and identified clearly by their coherent appearance in the wave field around the critical distances (large amplitude, critical reflections). Due to the relatively small number of seismic sources along each profile (~10 shot points), classical CMP like data processing failed to produce an image of the crustal reflectivity. Instead we used the automatic line-drawing migration approach of Bauer et al., (2013), which significantly enhances the quality and resolution of the image of the crustal structures. This technique automatically extracts coherent reflections in individual shot gathers, resulting in a set of line-drawing elements for every shot gather. These elements are characterized by different attributes: travel time, distance from shot, dip (slope or apparent velocity), semblance (a coherency measure) and amplitude, but no phase information is kept. These line-drawing elements are then migrated using the technique of Bauer et al. (2013) employing the velocity model previously derived by travel time tomography of refracted phases thus resulting in a consistent picture. Instead of showing the complete set of all migrated line-drawings (several thousands per shot gather), an automatic post-migration selection process has been applied (Bauer et al., 2013). Only line-drawing elements, for instance, above a given amplitude and semblance threshold, with specific dips (slopes, apparent velocities), etc. are selected. This selection significantly reduces the noisy appearance of the migrated shot gathers and puts emphasis on the sufficiently strong and coherent crustal reflections.

Due to the given geometry of sources and receivers, no near-vertical incidence reflections (e.g. from shallow or mid-crust) are imaged in the line drawing migration approach, only highly energetic wide-angle reflections from deeper reflectors (e.g. PmP phase) contributed to the image of crustal reflectivity (Figures 2, S3-S5).

FIGURE CAPTIONS:

Figure S1: Example of a shot record, profile 2, shot 4. Shown are all traces recording the shot (bandpass-filtered, trace-normalized). Note the direct Pg phase and the prominent PmP wide angle reflection at around 70 – 120 km / 4-6 s. Red dots indicate the travel times of the first arrivals, which have been picked and used during the tomographic inversion.

Figure S2: Overview of all 1921 travel time readings (picks of first P-wave arrivals) along profile 2. This dataset forms the input for the tomographic inversion of profile 2.

Figure S3: Results along profile 1. The top panel shows the tomographic Vp model, the lower panel shows the migrated line drawings (line segments) overlaid on the faded Vp model. For additional details see caption of Figure 2 of main document. The crustal structure along profile 1 seems to be more complex than along profiles 2 and 3 (Figure 2 of main document; Figures S4 and S5), with more lateral alternations of lower and higher velocities. We notice a broad region of moderate velocities along profile 1 beneath the Inner Makran unit which is much wider at this longitude (see Figure 1 of main document). In addition we also notice an anomaly of higher velocities (“D”) laterally sandwiched between lower-velocity regions (“C”) along profile 1. However, here anomaly “D” is not beneath the Outer Makran unit but shifted to the south. Thus, while the anomalies “C” and "D" along profiles 2 and 3 roughly coincide with tectono-stratigraphic units mapped at the surface, on profile 1 this association is not as obvious.

Figure S4: Results along profile 2. For details see captions of Figure 2 of main text and Figure S3.

Figure S5: Results along profile 3. For details see captions of Figure 2 of main text and Figure S3.

Figure S6: Results from the Monte Carlo travel time inversion: Distribution of Vp errors for the three profiles (lines as indicated). Red colors indicate regions of large Vp uncertainties (errors) in which no reliable velocities could be recovered because of poor or no ray coverage. These regions are clipped in the velocity models (Figure 2 of main document and Figures S3 – S5).

Figure S7: Synthetic recovery test. Bottom: Synthetic input model resembling the subducting plate, the backstop region (distances larger than 120 km) and some undulating high and low velocity anomalies within the forearc wedge. For this model all travel-times were calculated with a FD Eikonal solver using the same source and receiver geometry and travel time noise was added. Unresolved regions of the model are clipped (gray). Middle: Recovered structures revealed by the tomographic inversion of the synthetic travel time data. Top: Difference between synthetic and recovered model in percent. Note that the difference is below 5 % in the central part of the model indicating excellent recovery, increasing to values above 5 % for deeper parts and structures >140 km distance.

REFERENCES

Bauer, K., Ryberg, T., Fuis, G. S., and Lüth, S., 2013, Seismic imaging of the Waltham Canyon Fault, California: Comparison of Ray-Theoretical and Fresnel Volume Prestack Depth Migration, Bulletin of the Seismological Society of America, v. 103, no. 1, p. 340–352, doi:10.1785/0120110338.

Bodin, T. & Sambridge, M., 2009, Seismic tomography with the reversible jump algorithm. Geophysical Journal International, 178: 1411–1436. doi:10.1111/j.1365-246X.2009.04226.x

Bodin, T. , Sambridge, M., Rawlinson, N. & Arroucau, P., 2012, Transdimensional tomography with unknown data noise. Geophysical Journal International, 189: 1536–1556. doi:10.1111/j.1365-246X.2012.05414.x.

Haberland, C., Mokhtari, M, Ali Babaei, H, Ryberg, T., Masoodi, M., Partabian, A., & Lauterjung, J (2020): Data of the Western Makran Seismic Transects (Iran). GFZ Data Services. http://doi.org/10.5880/GIPP.201718.1

Kopp, C., Fruehn, J., Flueh, E.R., Reichert, C., Kukowski, N., Bialas, J., Klaeschen, D., 2000, Structure of the Makran subduction zone from wide-angle and reflection seismic data. Tectonophysics 329, 171-191

Ryberg, T. & Haberland, C., 2018, Bayesian inversion of refraction seismic traveltime data, GJI, doi: 10.1093/gji/ggx500.

Zelt, C. A., and P. J. Barton 1998, Three-dimensional seismic refraction tomography: A comparison of two methods applied to data from the Faeroe Basin, J. Geophys. Res., 103(B4), 7187–7210

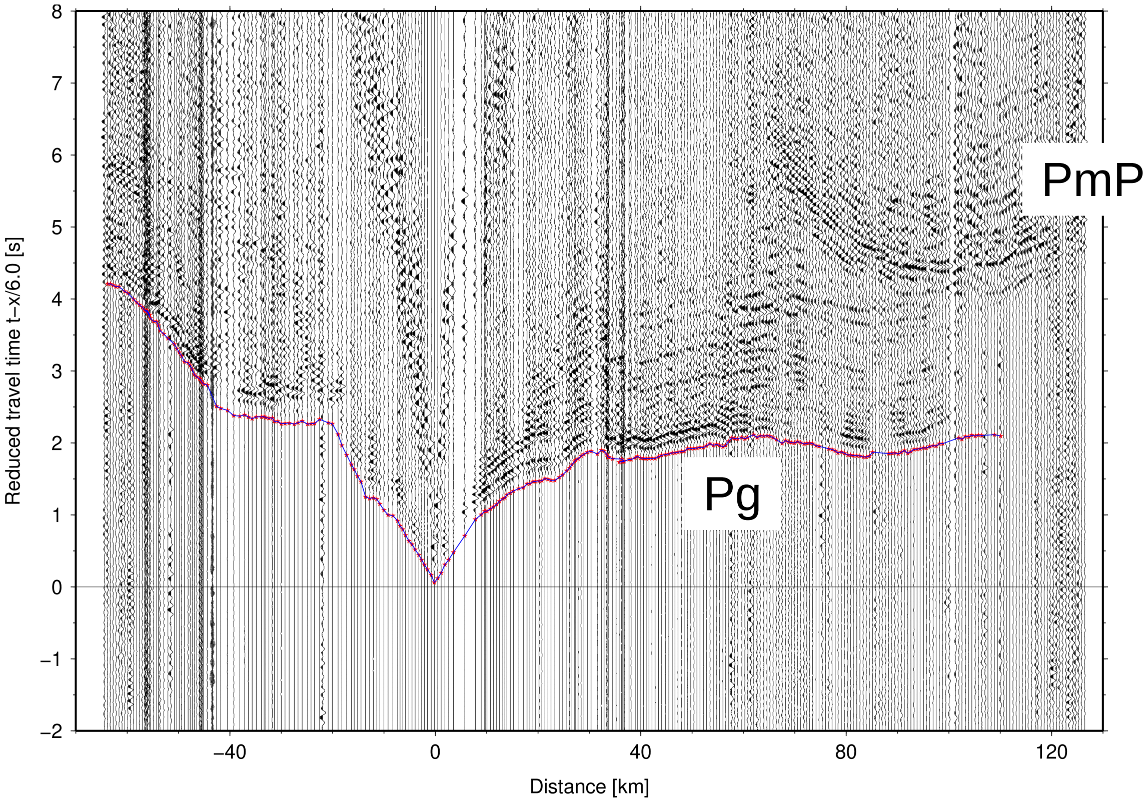
Reduced travel time t−x/6.0 [s]
Distance [km]
PmP
Pg
8
7
6
5
4
3
2
1
0
−1
−2
−40
0
40
80
120

Figure S1

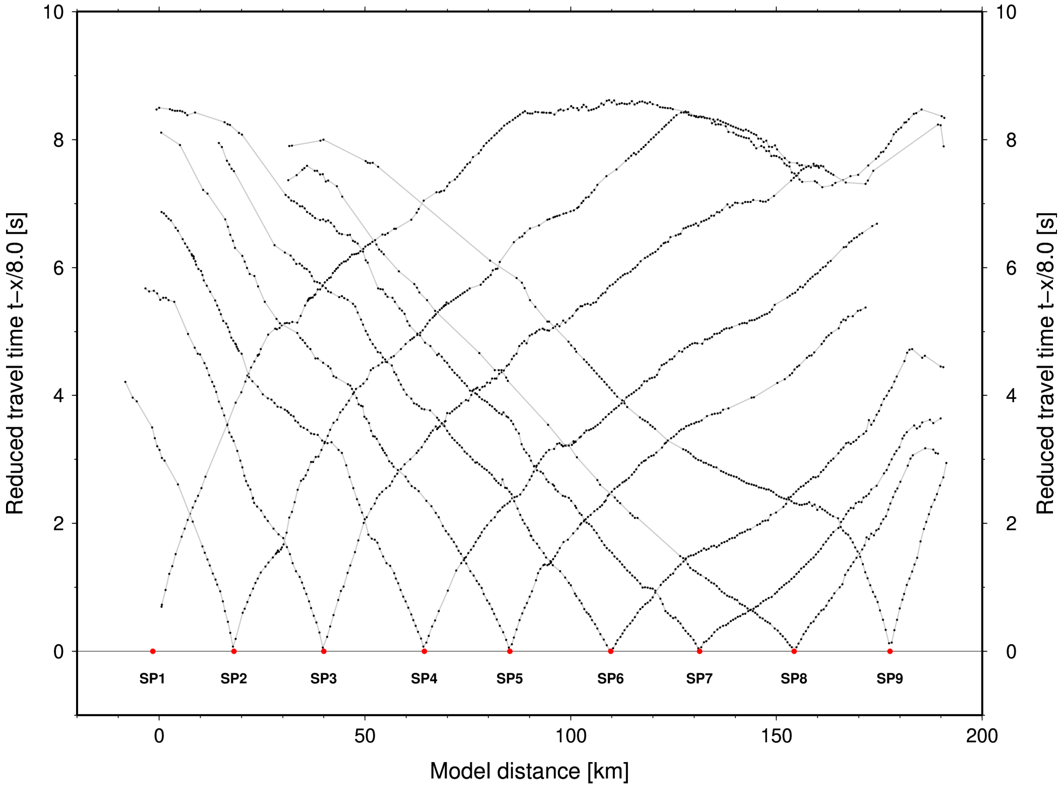
10
8
6
4
2
0
Reduced travel time t−x/8.0 [s]
SP1
SP2
SP3
SP4
SP5
SP6
SP7
SP8
SP9
0
50
100
150
200
Model distance [km]

Figure S2

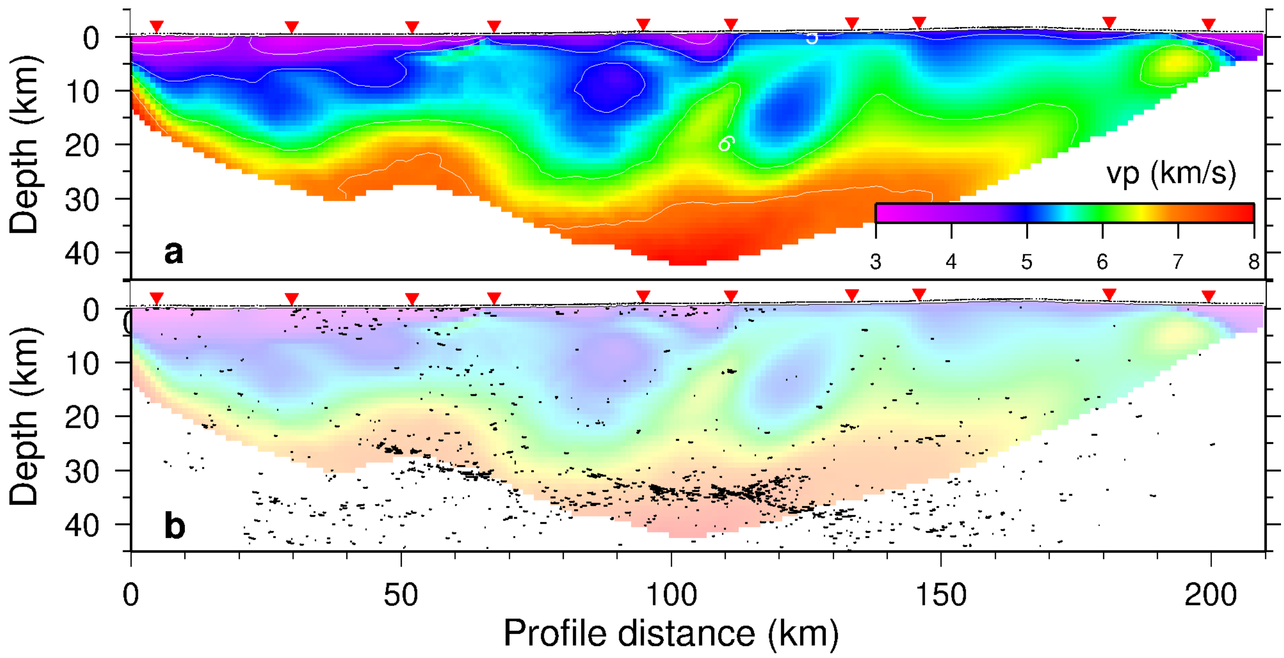

Depth (km)
a
b
vp (km/s)
3
4
5
6
7
8
0
10
20
30
40
0
50
100
150
200
Profile distance (km)

Figure S3

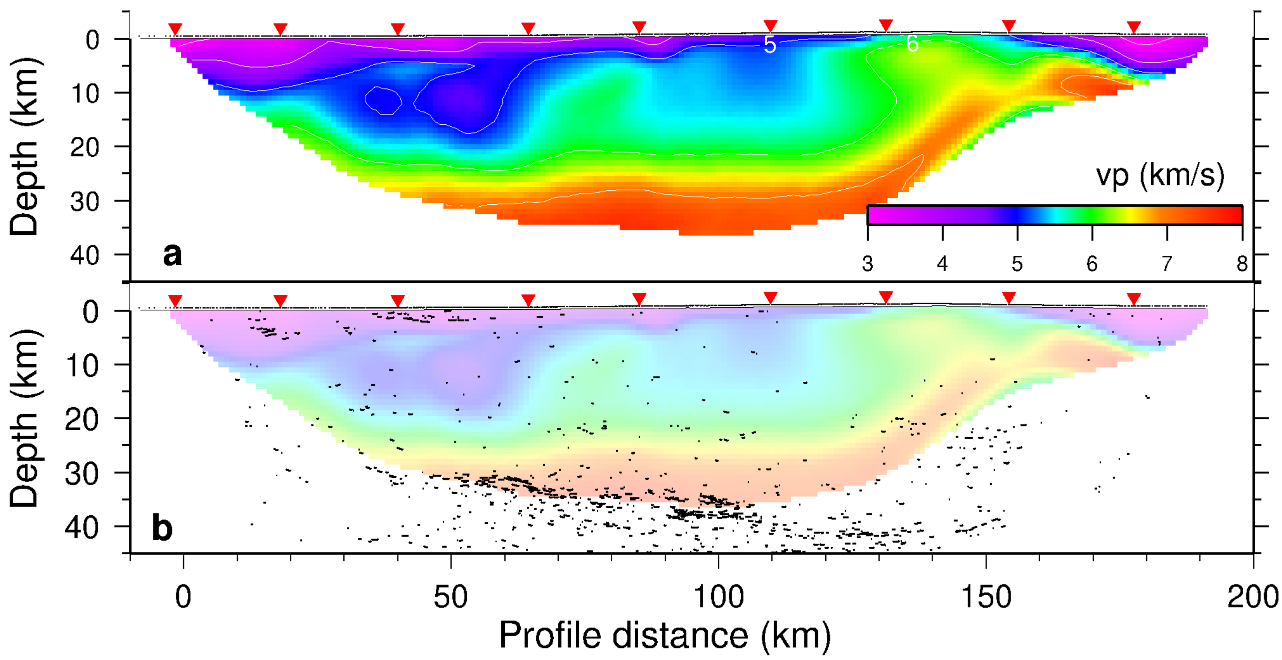

Depth (km)
0
10
20
30
40
5
6
vp (km/s)
3
4
5
6
7
8
a
b
0
50
100
150
200
Profile distance (km)

Figure S4

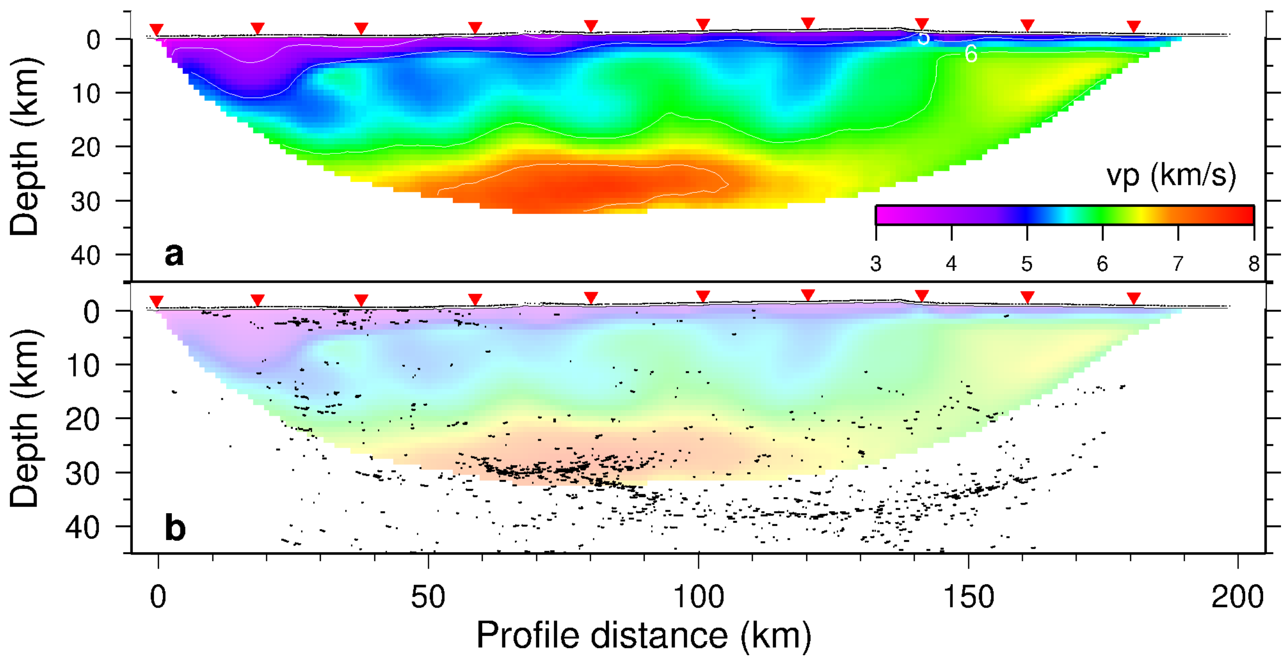
Depth (km)
0
10
20
30
40
5
6
vp (km/s)
3
4
5
6
7
8
a
b
0
50
100
150
200
Profile distance (km)

Figure S5

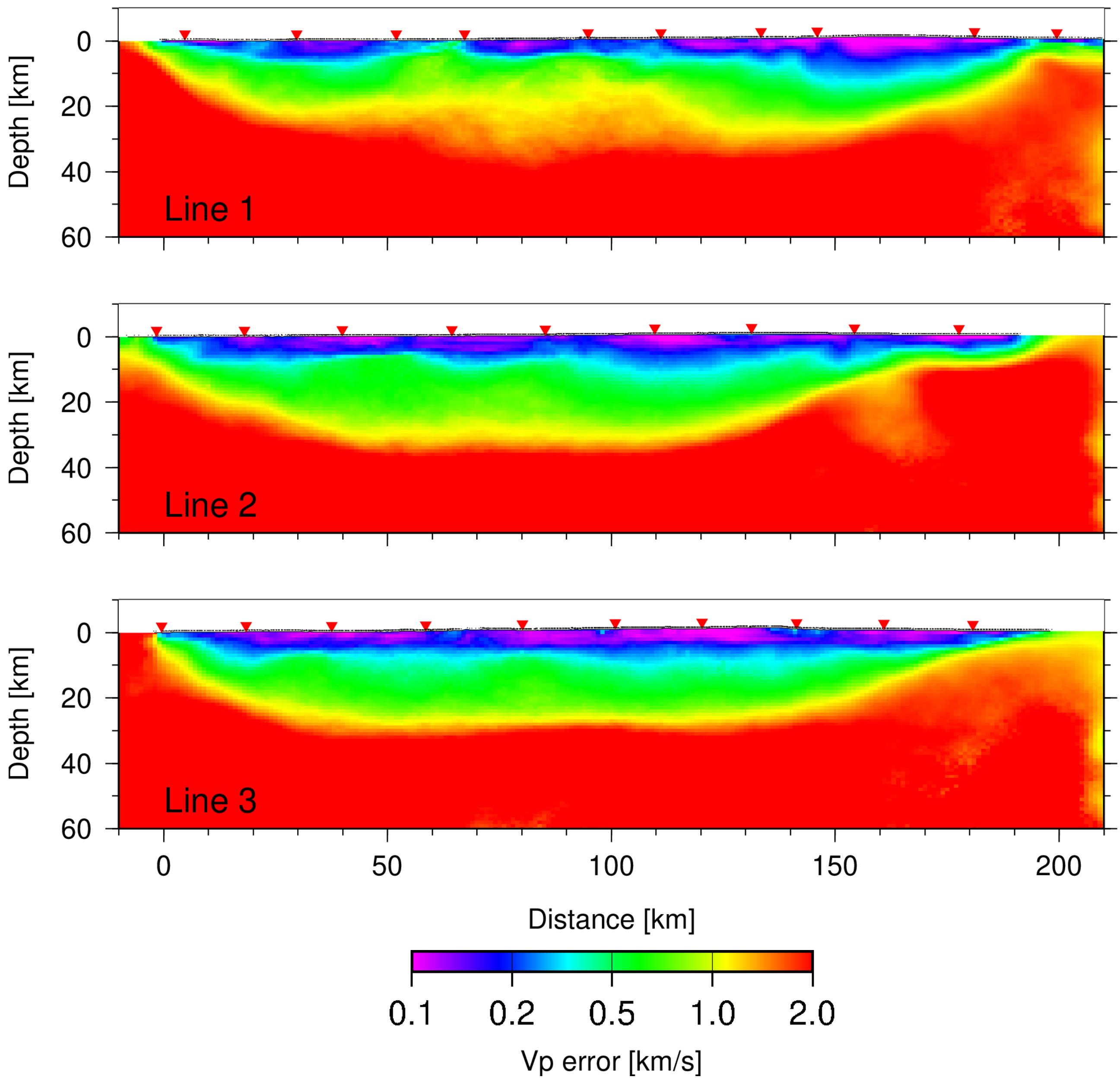

Depth [km]
0
20
40
60
Line 1
Line 2
Line 3
0
50
100
150
200
Distance [km]
0.1
0.2
0.5
1.0
2.0
Vp error [km/s]

Figure S6

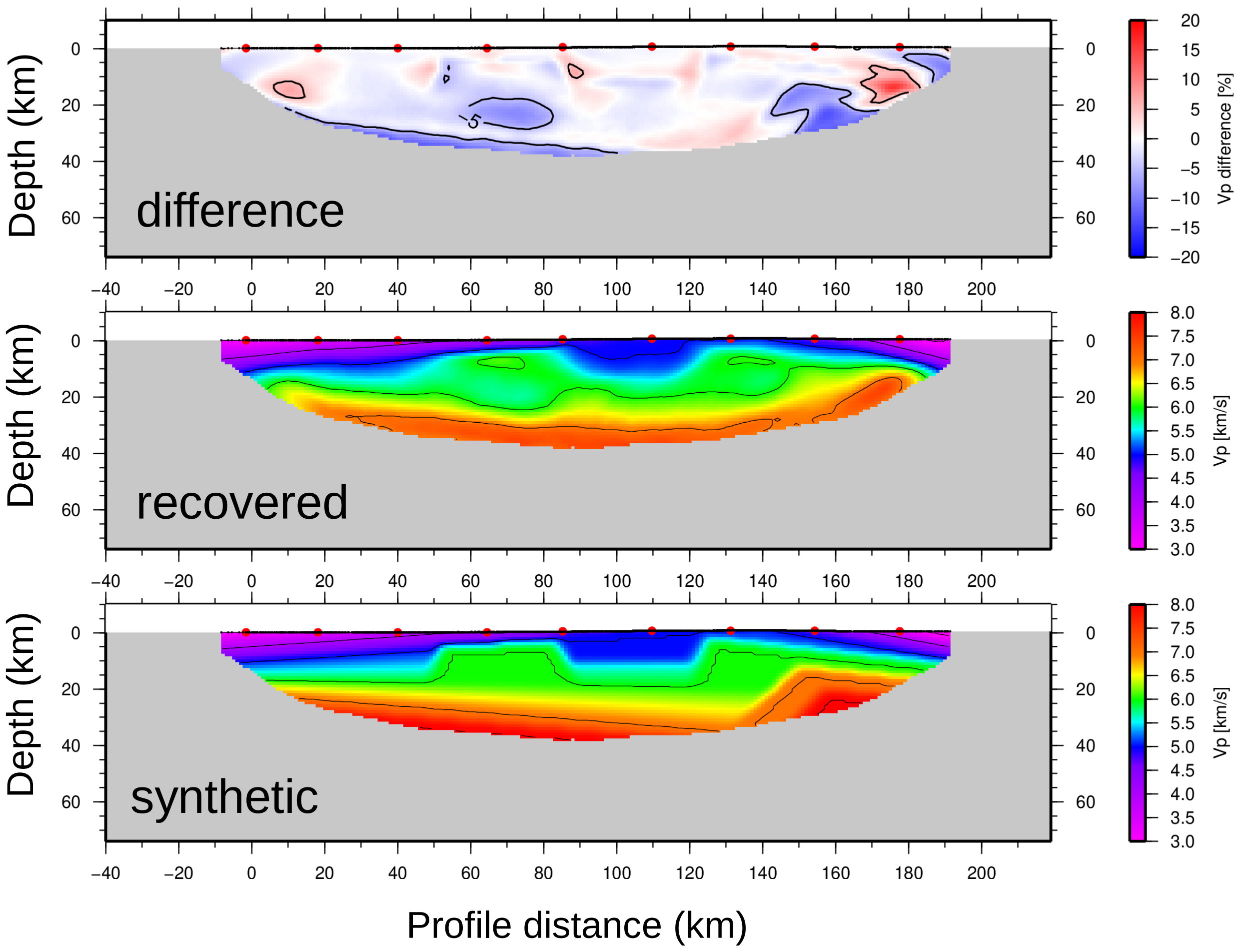
difference
recovered
synthetic
Depth (km)
Profile distance (km)
Vp difference [%]
Vp [km/s]
-5

Figure S7